Chemical functionalization of N-doped carbon nanotubes: a powerful approach to cast light on the electrochemical role of specific N-functionalities in the oxygen reduction reaction

Giulia Tuci,[a] Claudio Zafferoni,[b] Andrea Rossin,[a] Lapo Luconi,[a] Antonella Milella,[c] Matteo Ceppatelli,[ad] Massimo Innocenti,[b] Yuefeng Liu,[ef] Cuong Pham-Huu[e] and Giuliano Giambastiani*[ag]

[a] Institute of Chemistry of OrganoMetallic Compounds, ICCOM-CNR and INSTM Consortium, 50019 Sesto F.no, (Florence), Italy. Fax: +39 055 5225203; Tel: +39 055 5225288;
E-mail: giuliano.giambastiani@iccom.cnr.it

[b] Department of Chemistry, Univ. of Florence, 50019 Sesto F.no, Florence, Italy

[c] Department of Chemistry, Univ. of Bari, 70126 Bari, Italy

[d] LENS, European Laboratory for Non-linear Spectroscopy, Via N. Carrara 1, I-50019 Sesto F.no, Florence, Italy

[e] Institut de Chimie et procédés pour l'Energie, l'Environnement et la Santé (ICPEES), UMR 7515 CNRS-Université de Strasbourg, Strasbourg, France

[f] Shenyang National Laboratory for Materials Science, Institute of Metals Research, Chinese Academy of Sciences, 72 Wenhua Road, Shenyang, Liaoning, 110016, China

[g] Kazan Federal University, 420008 Kazan, Russian Federation

Dedicated to Professor Giovanni Poli on the occasion of his 60th birthday.

Abstract

In this paper, we describe the combination of two different synthetic approaches to carbon nanotube N-decoration/doping: the chemical functionalization with tailored N-pyridinic groups and the classical Chem- ical Vapor Deposition (CVD) technique. Accordingly, CVD-prepared N-doped CNMs (NMWs) and their N-decorated (chemically functionalized) counterparts (NMW@$N_{1,2}$) have been prepared and used as metal- free electrocatalysts for the oxygen reduction reaction (ORR). It has been demonstrated that chemical functionalization occurs on the NMW surface sites responsible

for their inherent electrochemical properties and "switches them off". As a result, the ORR promoted by NMW@$N_{1,2}$ is fully controlled by the appended N-heterocycles. A comparative analysis of N-functionalized samples and N-doped (CVD prepared) materials is used to foster the hypothesis of a unique N-configuration (N-pyridinic) responsible for the overall electrochemical performance in NMWs. In addition to that, original electrochemical insights unveiled during the study are discussed and the truly metal-free action of NMW in ORR catalysis is demonstrated.

1. Introduction

The development of cheap, highly efficient and durable electrocatalysts for the kinetically sluggish

oxygen reduction reaction (ORR) is a challenging issue for sustainable development of devices at the

heart of renewable energy technology

i.e. metal–air batteries and fuel cells.[1–4] Although platinum and its alloys have traditionally been

regarded as the best catalysts for the process,[5] their prohibitive costs along with the limited reserves

in nature largely limit their widespread exploitation in the market. Moreover, Pt-based

electrocatalysts suffer from severe poisoning effects (such as gas adsorption or fuel crossover) which

affect their durability and limit their practical application.[6–9] Along with recent intensive research

efforts in reducing or replacing Pt-based electrocatalysts in the ORR,[10] light heteroelement doped

carbon nanomaterials (CNMs) with at least one dimension tailored at the nanometer scale have

increased interest of the catalysis and materials science community.[1,3,11–18] In particular, nitrogen-

doped CNMs (N-CNMs) have been intensively investigated as metal-free systems in light of their

remarkable electrochemical properties in the ORR in both alkaline[3,19,20] and acidic[21] environments. It

is generally accepted that the inherent catalytic performance of N-CNM catalysts originates from the

electronic charge redistribution in the final material induced by the heteroelements.[16,18] Several

studies have discussed how the N-doping and the relative N-configurations (i.e. N-pyridinic, N-

pyrrolic, N-quaternary, N-oxide as in-plane or edge-sites) would increase the electronic density of

states near the Fermi level, thus facilitating the electron transfer from the bands of the C network to

the antibonding orbitals of the surface activated O_2.[22–25] Despite these contributions, a practical

solution to the material surface N-doping control (in terms of N-configuration and N-loading) is still

far from being exhaustively accomplished. Chemical Vapor Deposition (CVD) remains the most

effective and widely used technique for the large scale N-CNM production.[26,27] Other techniques such

as CNM annealing in the presence of different nitrogen sources,[28–30] chemical reduction/doping with

selected N-containing reducing agents[12,31,32] or direct carbonization of N-containing organic

precursors[33–35] constitute valuable and alternative synthetic paths. Despite their feasibility, all these

processes generate N-CNMs containing different N-configurations where the adjustment of their relative per- centages in the final sample (by thermal treatment) remains the only tunable parameter. As a consequence, it is difficult to draw up any conclusion on the role of the different N-configurations[25,30,35–46] as well as on that of the total N-loading on the final electrocatalyst activity.[47–50] What is generally accepted is that N-sites located at the graphitic edge planes[36,46,51] give the strongest contribution to the ORR process. Accordingly, a 4e−reduction path takes place prevalently on the edge-type N-sites i.e. N-pyridinic and N-quaternary ("valley N-graphitic"). While the former is supposed to control the overpotential value at which the ORR starts (Eon), the latter is claimed to regulate the catalyst's limiting current density values (JD).[30] On the other hand, in-plane N-defects are responsible for the occurrence of 2e−processes, preferentially.[52]

Recent studies from our group have proposed a conceptually new approach to the nanomaterial N-decoration via chemical functionalization of pristine CNMs with tailored N-containing groups.[53,54] This methodology has provided catalysts with excellent ORR performance and it has contributed to establish the role of specific N-functionalities for the O_2 activation and their subsequent electrochemical conversion. In particular, pyridine nuclei in a well-defined electronic environment have demonstrated a key role on the Eon improvement as well as on the control of the average number of electrons transferred per mol of O_2 throughout the electrochemical process.[54]

The objective of the present study is to provide a clear-cut understanding of the complex structure–reactivity relationships that drive the electrocatalytic performance of classically CVD-prepared N-doped CNTs as metal-free systems for the ORR. To this aim, CVD-prepared N-doped MWCNTs (NMWs) and their N-decorated (chemically functionalized) counter- parts (NMW@N1,2) have been prepared, completely characterized and electrochemically compared. The study has offered valuable hints to unveil the effective nature of the active sites present in the complex NMW materials and directly engaged in the catalytic ORR process. A careful analysis of the surface properties of all synthesized samples is finally used to unveil original electrochemical outcomes.

For the sake of completeness, it should be mentioned that recent literature findings have revealed the

non-innocent role in ORR catalysis played by metal residues coming from the NMW synthesis.[55,56] In this study we provide evidence of the truly metal-free action of NMW in ORR, ruling out any possible contribution from metal contaminants.

2. Experimental

2.1 General considerations

All manipulations dealing with the chemical functionalization of NMW and MWCNT were carried out un- der a dry nitrogen atmosphere using standard Schlenk-type techniques. Nitrogen (>99.999%; Rivoira) was dried through a $CaCl_2$ column and deoxygenated with an oxysorb cartridge from Messer Griesheim prior to use. oDCB (o- dichlorobenzene) and CH_2Cl_2 (dichloromethane) were dried according to the literature procedures[57] and stored under a nitrogen atmosphere. Dry acetonitrile (CH_3CN) was obtained by means of an MBraun Solvent Purification System. MWCNTs (98% in C) were purchased from Sigma-Aldrich (lot. no. MKBH5814 V) and used as received. Unless other- wise stated, all other chemicals were purchased from commercial suppliers and used as received without further purification. For each functionalized sample (NMW@$N_{1,2}$, MWCNT@Acr^{OX}), a "blank functionalization test" was performed using identical reaction conditions except for the use of the isopentyl nitrite reagent.

The NMW sample was prepared by Chemical Vapor Deposition (CVD) with minor modifications to the literature procedure.[58] Iron nanoparticles (20 wt%) over Al_2O_3 (Aeroxide AluC) are used as a catalyst to promote the CVD process in combination with ethane (C_2H_6) and ammonia (NH_3) as the C- and N-sources, respectively. Argon (Ar) is the inert carrier for the two gaseous feedstocks and a 50 : 50 : 50 sccm (C_2H_6 : NH_3 : Ar) flow rate is set-up in a reactor pre-heated at 750 °C to grow the sample. Catalyst (Fe/Al_2O_3) removal is fully accomplished through a prolonged basic–acidic material work- up under severe reaction conditions which can exclude any relevant contribution from exposed metal-traces to the inherent material catalytic properties (*vide infra*).

Electrical conductivity measurements on the NMW and NMW@N_2 samples were

prepared as follows: 30 mg of each sample was suspended in 10 mL of ethanol and soni- cated for 30 min to get a homogeneous material dispersion. Afterwards, the suspension was filtered under vacuum on a PTFE filter (Whatman®) with a 0.2 μm pore size. The filter containing the CNT-sample was then dried under vacuum at 50 °C for two hours until a self-standing CNT Buckypaper separated off. The thickness of the Buckypaper films was measured using a micrometre screw gauge. For the measurement of the material resistivity (ρ) a four-point probe method was used.[59] The set-up consists of four point collinear probes. A constant current of 1 mA was then applied on the two outer probes and the voltage drop was measured at the inner probes (see also Table S3, ESI). All measurements were run at 295 K. RRDE measurements on the blank samples have excluded any electrochemical activity associated with potentially physisorbed N-containing heterocycles.[53,54] Furthermore, any electrochemical activity (RRDE measurements) potentially associated with reagent and solvent contaminations has been properly ruled out using a blank test conducted on MWCNTs treated with isopentyl nitrite in a oDCB/CH_3CN mixture. For the synthesis of the 9-aminoacridine N-oxide, see the ESI.

2.2 General procedure for the NMW and MWCNT functionalization via aryldiazonium salt chemistry

In a typical procedure, 40 mg of the nanomaterial (NMW or MWCNT) is weighed into a two-necked 100 mL flask and suspended in 32 mL of dry and degassed oDCB. The suspension was sonicated for 30 min and then treated with a degassed acetonitrile solution (16 mL) of the corresponding aniline (0.86 mmol). Isopentyl nitrite (0.17 mL, 1.30 mmol) was added via syringe, and the suspension was further sonicated for 10 min. The mixture was heated at 80 °C for 14 h under stirring and a nitrogen atmosphere. Afterward the mixture was cooled to room temperature, diluted with ethyl acetate (20 mL), and sonicated for 20 min before being centrifuged to recover the solid residue. The latter was then washed with ethyl acetate and then twice with dichloromethane, each time sonicated for 10 min and separated from the supernatant by centrifugation. For the work-up procedure of the

MWCNT@Acr^{OX} sample, the recovered solid was washed several times with MeOH in order to remove all unreacted reagent. The solid residue was finally suspended in dichloromethane (MeOH for the MWCNT@Acr^{OX} sample), sonicated for 20 min, and filtered through a 0.2 μm pore PTFE filter. The collected material was dried at 50 °C under vacuum to constant weight and stored in air at room temperature.

2.3 Thermal treatment of NMW to afford the r-NMW sample

150 mg of NMW are placed in a sealed quartz tube and put under vacuum for 1 h. Afterwards, the tube was filled with Ar and the sample was heated at 350 °C for 1 h (heating rate: 5°C min^{-1}) while maintaining a constant stream of Ar throughout the heating. After cooling the sample to room temperature, the solid was recovered and stored in air at rt.

2.4 Material characterization and analysis conditions

Thermogravimetric Analyses (TGA)

Analyses were performed under either N2 or air atmosphere (100 mL min−1) on an EXSTAR Thermo Gravimetric Analyzer (TG/DTA) Seiko 6200.

X-ray Photoelectron Spectroscopy (XPS)

Analyses were performed with a Thermo Fisher Theta Probe spectrometer equipped with a monochromatic Al Kα X-ray source (1486.6 eV) with a spot size of 300 μm, corresponding to a power of 70 W and at a takeoff angle of 53° relative to the sample nor- mal. Samples in the form of powders were fixed on ultrahigh vacuum compatible Cu adhesive tape (3M) ensuring, as much as possible, a uniform coverage. Survey spectra (0–1300 eV) were acquired at a pass energy of 200 eV with an energy step size of 1 eV. High resolution spectra were recorded at a pass energy of 100 eV with a step size of 0.05 eV. In the set condi- tions the overall energy resolution was 0.9 eV. When needed, charge compensation for the treated MWCNTs was accomplished by a low energy electron flood gun (1 eV). Charge correction of the spectra was performed by taking the sp^2 graphitic component of the

C 1s spectrum as internal reference (binding energy, BE = 284.6 eV). Special care was devoted during the analyses, to verify that no change in the samples was induced by exposure to the X-ray beam and the electron flood gun. XPS analysis was repeated on three different spots for each sample. High resolution spectra of detected elements were acquired for quantitative and detailed BE chemical shift analysis. Atomic percentages were calculated using the Scofield sensitivity factors set in Thermo Avantage V4.87 software (Thermo Fisher Corporation) and a nonlinear Shirley background subtraction algorithm. The high resolution spectra were fitted with mixed Gaussian–Lorentzian peaks after a Shirley background subtraction. The determined standard deviation in the peak position was ±0.2 eV.

Raman spectroscopy

Spectra were recorded in a back scattering configuration using 0.5–1.5 mW of the 647.1 nm wavelength of a Kr ion laser, after carefully excluding any photochemical effect on the sample. The scattered radiation was focused ($\sim$5μm) and collected by a microscope objective (Mitutoyo, 20×), spatially filtered, dispersed by a single stage monochromator(Acton Trivista) equipped with a 900 grooves mm grating and recorded by a nitrogen cooled CCD detector (Princeton Instruments), with a resulting spectral resolution of 1.5cm^{-1}.[60] Samples were prepared depositing the synthesized materials as fine powders on a metal holder. Each sample was randomly probed on at least three different positions and consistent data were obtained. Raman spectroscopy was employed to get insight into the effect of N-decoration on the C framework of the investigated materials by the changes in the intensity ratio of the D (1360 cm^{-1}) and G (1590 cm^{-1}) bands. After background subtraction the Raman spectra were fitted using Voigt line shapes, and the integrated intensities of the D- and G-peaks were used for the calculation of the ID/ IG ratios.[61–63]

Transmission Electron Microscopy (TEM)

Analyses were performed by using a Philips CM12 microscope operating at 120 kV, on samples prepared by drop-casting previously sonicated suspensions (EtOH) over copper grids coated with a

Formvar film (FF200-Cu-Formvar film only). TEM images were recorded with a CCD camera (Gatan 791). The Brunauer–Emmett–Teller (BET) specific surface area (SSA) was measured on an ASAP 2020 Micromeritics instrument, using N_2 as absorbent at liquid-N_2 temperature (77 K). The NMW and r-NMW samples were completely degassed/activated at 250 °C for 14 h (Fig. S5, see the ESI).

Electrical conductivity

Measurements on thin films of NMW and NMW@N_2 were run with a four-point probe method using a potentiostat/galvanostat Amel mod 750 to control the current and a potentiostat/galvanostat Parstat 2273 to register the potential through an open circuit potential (OCP) experiment (Table S3). Rotating-Ring Disk Electrode (RRDE). Measurements were performed using a ring-disk electrode from Pine Instrument Co. consisting of a glassy carbon (GC) disk insert (ø 5 mm; A = 0.196 cm^2) and a Pt ring (A = 0.11 cm^2). The RRDE measurements were carried out using a modulated speed rotator (MSR) from Pine Instrument Co. All the measurements were carried out using an Autolab bi-potentiostat/ galvanostat in a single compartment glass cell using a three- electrode arrangement. The working electrode was prepared as follows: an appropriate amount of CNTs (10 mg) was dispersed in 0.220 g of water, 0.112 g of ethanol, and 0.084 g of a Nafion solution (5 wt% in lower aliphatic alcohols and water). The resulting ink was sonicated for 30–45 min and drop-cast onto the glassy carbon electrode (3 mg). The as-prepared electrode was then dried at room temperature. A platinum wire was used as a counter electrode, and a double junction Ag/AgCl/KCl sat. electrode served as a reference electrode. All CV and RRDE experiments were carried out at a scan rate of 5 mV s^{-1} in the potential range from either −1.1 to 0.2 V or 0.2 to −1.1 vs. Ag/AgCl/KCl sat. Nitrogen or oxygen was used to purge the solution to achieve an oxygen-free or an oxygen- saturated electrolyte solution, respectively. A commercial Metrohm Pt electrode (ø 3 mm) was used for comparison, and all measurements were repeated at least four times. Finally, the measurement setup, the moderate electrolyte viscosity, and the entity of the measured currents did not require any ohmic compensation. All prepared CNT inks were indefinitely stable in air for

months with neither any apparent decomposition nor alteration of their electrochemical performance. The number of electrons transferred per O_2 molecule (n) in the ORR for the different catalysts has been calculated by the Koutecky–Levich equation applied to the ORR curves obtained at different rotation rates (rpm).[64] For the electrochemical data processing see the ESI.

Elemental analyses

Analyses were performed using a Thermo FlashEA 1112 Series CHNS-O elemental analyzer, and elemental average values were calculated over three independent runs. Temperature-programmed decomposition (TPD-MS) measurements and carboxylic function loading quantitative analysis. The TPD- MS analyses on the NMW and r-NMW samples were performed using a Hiden Analytical CATLAB® instrument (http://www.hidenanalytical.com). Thermal CO_2 evolution from the samples is carried out under an argon flow (flow rate = 20 mL min^{-1}) in the 25–350 °C temperature range (sample heating rate = 5 °C min^{-1}). The blank experiment has been carried out using the sample holder filled with glass wool only, under a 5% CO_2 in argon flow. The same flow rate has been setup, at the constant temperature of 25 °C and for a total time of 60 minutes. An ideal gas behavior for CO_2 has been considered to calculate the moles of CO_2 sent to the mass detector in this experiment (1 mol = 22.414 L). The quadrupole mass detector limit is 2×10^{-14} torr. The amount of gas released in a specific time interval can be inferred from the (known) gas flux. This quantity is proportional to the area lying underneath the m/z vs. t plot. The TPD Plotter® software[65] integrated in CATLAB easily provides numerical values for this area. Thus, the exact amount of CO_2 released could be calculated through a simple proportion between the "blank" graph area and that coming from Fig. 4A.

Acid–base titration of pristine and functionalized samples

Five milligrams of the selected N-decorated material was suspended in 7 mL of a standard HCl solution (2.8×10^{-3} M, standardized with Na_2CO_3 as primary standard), sonicated for 30 min, and maintained in the dark at rt under stirring for 48 h. Afterward the suspension was centrifuged, and

three aliquots of the supernatant solution were titrated with a standardized solution of NaOH (2 × 10^{-3} M). The N-basic site content (N%) was calculated for each sample as the average value over three independent runs.[66,67]

3. Results and discussion

3.1. Synthesis and characterization of in situ N-doped CNTs (NMW) and their chemically N-decorated counterparts (NMW@N$_{1-2}$)

The NMW sample is classically prepared by a chemical vapor deposition (CVD) technique, using a procedure similar to that previously reported by some of us (see the Experimental section).[58] The N-content (bulk) of the NMW sample is fixed to ≈ 3.2% as measured by elemental analysis (EA) (Table S1). The high resolution XPS N 1s core region (Fig. 1), analyzed with the best fitting procedure, highlights the complexity of the N-composition for the as-synthesized material: three main components at 398.5 (23.0%), 401.4 (35.5%) and 404.9 eV (22.1%) are attributed to pyridinic[68–71], quaternary[69,72,73] nitrogens and N-oxide species,[74] respectively.
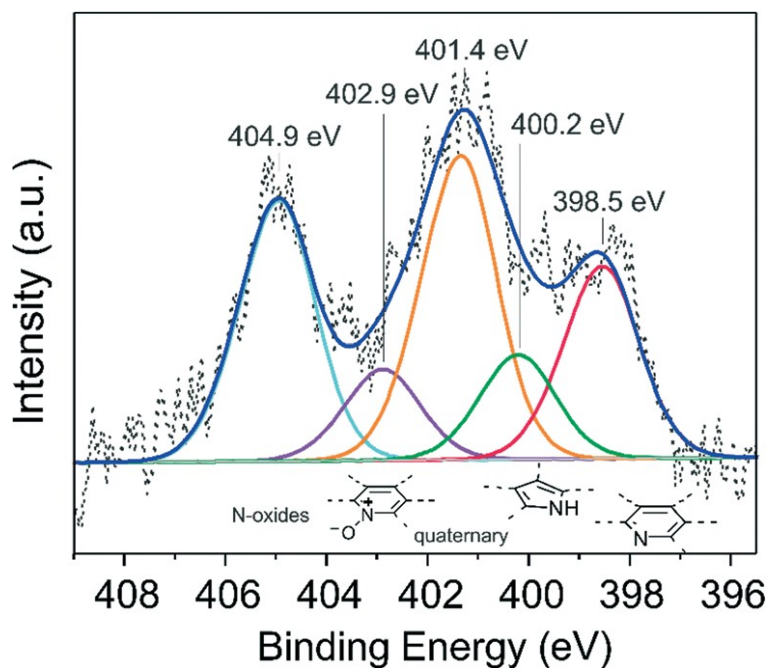

Figure 1. High resolution XPS N 1s core level region of NMW and its relative curve fitting.

The chemical functionalization of NMW with N-containing groups[53,54] is carried out with

the aim of 1) increasing the material surface N-content and 2) getting insights into the nature of the active sites in NMW responsible for its electrochemical activity in ORR (*vide infra*).

Taking advantage from our previous studies,[53] acridine and pyridine groups are selected as model N-containing functionalities for the NMW chemical decoration (Scheme 1).
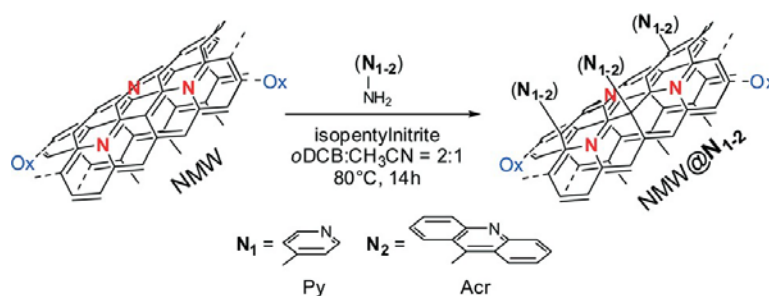
Scheme 1 NMW N-decoration via aryldiazonium salt (Tour) protocol. Samples N1 and N2 have also been employed in the N-decoration of "fully C" multi-walled carbon nanotubes (MWCNTs). See ref. 53 and 54.

The covalent surface modification is performed via aryldiazonium salt chemistry (Tour protocol).[77–84] As Scheme 1 shows, the NMW functionalization occurs under relatively mild conditions in the presence of a para-aniline derivative of a selected N-containing group (N1 = pyridine; N2= acridine) and isopentylnitrite. Each functionalized sample undergoes a careful work-up procedure where successive sonication/centrifugation and filtration cycles are used to remove all unreacted reagents. A blank test (in the absence of the iso-pentylnitrite reagent) is also carried out with each aniline derivative to assess the complete removal, after material work- up, of any residual amount (traces) of simply physisorbed N- contaminants.

Qualitative evidence of the functionalization that occurred is provided by TG analysis of the N-decorated NMW samples (Fig. S1, C–D, see the ESI). Both materials show a gradual decomposition trend in the 40–750 °C temperature range under a N_2 atmosphere. More marked weight losses, ascribed to the progressive removal of the surface O-containing functionalities as well as chemically grafted $N_{1–2}$ groups, are measured in the 150–400 °C temperature range. At higher temperatures, the curves show largely superimposable decomposition profiles and similar to that of the plain NMW

sample. Finally, TGA of the blank tests show superimposable profiles that accounts for a complete removal of any simply physisorbed reagent or solvent (Fig. S1B, see the ESI). XPS measurements give additional support to the material N-decoration that occurred. The N 1s core level spectra of the NMW@N$_{1-2}$ materials (Fig. S2A and B, see the ESI vs. Fig. 1) show appreciable increases of the 398.8 eV component, consistent with an increased content of the pyridinic nitrogen in both samples (NMW@N$_1$: 37.8%; NMW@N$_2$: 32.6%). Finally, an overall increase of the N-content to 4.68 and 4.76% is measured by EA on the NMW@N$_1$ and NMW@N$_2$ materials, respectively (Table S1).

In terms of material morphology, Raman and TEM measurements conducted on all functionalized samples are consistent with the non-invasive character of the N-decoration procedure. Indeed, the covalent grafting of N-containing groups to the outer surface of NMW leaves its morphological properties virtually unchanged. The Raman spectra of NMW and NMW@N$_{1-2}$ do not reveal any major alteration of the crystallite and defect site surface density and the measured intensity ratio of the D and G modes (I$_D$/I$_G$) falls in a very narrow range (Fig. S3, see the ESI). Similarly, TEM micrographs of the functionalized materials (NMW@N$_1$, NMW@N$_2$) do not present any major morphological change compared with the pristine NMW sample; neither variations in terms of tube length and diameter nor modifications of the bundle aggregation degree are observed for the two functionalized materials on the whole scanned area (Fig. S4, see the ESI).

One main difference between the N-functionalized materials (NMW@N$_{1-2}$) and the pristine NMW sample deals with their acid/base properties. The basic character of the N-decorated materials (NMW@N$_{1-2}$) is measured by acid–base titration and it accounts for the contribution of the grafted heterocycles available to the material surface only. Indeed, the influence of the NMW core on the overall material basicity is negligible. This is confirmed by the acid–base titration of the plain NMW where no titratable basic sites are virtually present (Table S2). At odds with a relatively large component of pyridinic groups in NMW (Fig. 1), none of them seems to be definitively available at the outer material surface.[85] This finding can be explained with the work-up conditions applied to the

purification of the CVD prepared NMW sample. A prolonged material treatment under severe and even oxidative conditions changes the chemical composition of the outer material surface dramatically. In particular, the NMW heating in refluxing nitro-hydrochloric acid (aqua regia) readily and irreversibly converts those chemically accessible and basic N-groups (including N-pyridinic) into their N-oxide counterparts. Electrochemical comparative studies between all N-containing materials (NMW and NMW@N_{1-2}) are engaged with the aim of shedding light on the electrochemical role in ORR of specific N-functionalities of the complex NMW sample. In addition, original electrochemical insights into the structure–reactivity relationship of the CVD prepared sample (NMW) have been unveiled.

3.2 Rotating ring-disk electrode (RRDE) measurements on the in situ prepared sample (NMW) and its N-functionalized counterparts (NMW@N_{1-2})

For all nanotube samples, a well sonicated EtOH/H_2O/Nafion®-based ink is prepared and subsequently cast on a rotating glassy carbon (GC) electrode to provide a thin and homogeneous film after solvent evaporation (see the Experimental section for details). The as-prepared electrocatalysts have been investigated by cyclic voltammetry (CV) using a three-electrode cell operating in a 0.1 M KOH solution and consisting of an Ag/AgCl/KCl saturated reference electrode and a Pt-wire counter-electrode. As shown in Fig. S6 (see theESI), all samples under O_2-saturated conditions show a well- defined ORR cathodic peak not present under a N_2 saturated environment. Similarly, rotating ring disk electrode (RRDE) voltammograms are acquired for all samples in an O_2-saturated 0.1 M KOH electrolyte solution and compared with the bare glassy-carbon (GC) and the commercial Metrohm Pt- polycrystalline electrode (Ø 3 mm). For all nanomaterials, the total amount of the deposited solid catalyst is fixed to 358 μg cm^{-2}, a value that is arbitrarily established in accordance with the highest number of electron transfer measured from three separate electrocatalysts prepared at variable NMW ink loadings (see Table S4). Linear sweep voltammograms are recorded for each sample at different spin rates (from 400 to 2000 rpm), while sweeping potentials linearly

from −1.1 to 0.2 V and reversing them against Ag/AgCl/KCl sat. (Fig. S7, see the ESI); for all the electrochemical profiles, background currents measured under saturated N_2 conditions at the same potential scan rate (5 mV s^{-1}) are subtracted from the respective curves to eliminate all the capacitive contributions.

Fig. 2A shows the ORR polarization curves recorded at 800 rpm for NMW and its N-functionalized counterparts (NMW@N_{1-2}) along with the respective ring current values relative to the oxidation of hydrogen peroxide ions (HO$_2$$^-$) at the Pt-ring electrode (Fig. 2A′).
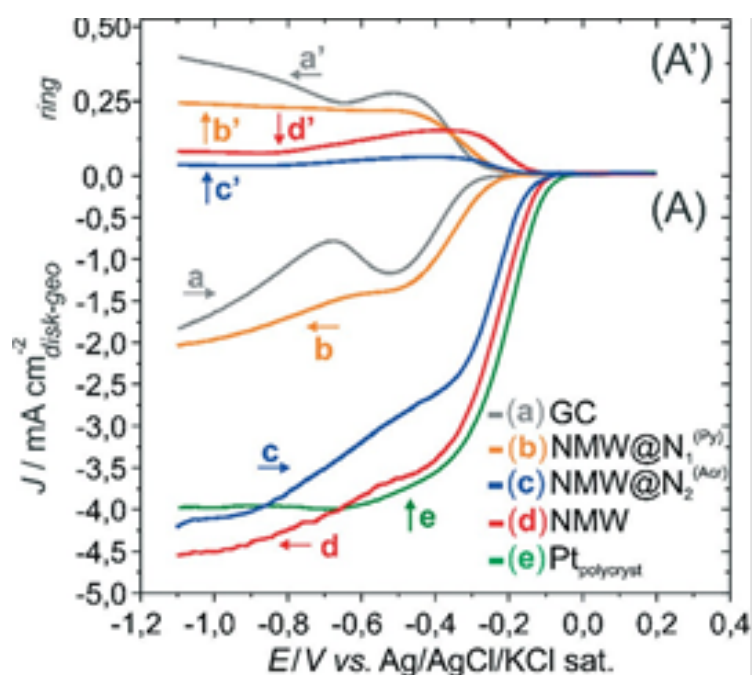

Figure 2. (A) RRDE current–potential curves at 293 K for ORR in an O_2 saturated 0.1 M KOH solution recorded by using a rotating ring-disk GC electrode [GC disk, A = 0.196 cm^2] with (A′) a Pt ring [A = 0.11 cm^2] held at a potential of 0.50 V. All samples are measured at an angular rotation rate (f) of 800 rpm with a scan rate of 5 mV s^{-1}.

RRDE current–potential curves measured for the bare GC and the commercial Pt-polycrystalline electrode under identical conditions are also shown for the sake of comparison. The onset potential (E_{on}) values measured for the NMW sample and its N-decorated counterparts (NMW@$N_1^{(Py)}$ and NMW@$N_2^{(Acr)}$) are negatively shifted from that of Pt with marked differences in terms of E_{on} and J_D (curve c vs. b). The NMW catalyst shows excellent ORR performance (around 20 mV overpotential for the Eon value compared with Pt) with a voltammetric profile very close to

that recorded for the reference Pt-based system and even higher limiting current density (J_D) values at higher overpotentials. As a distinctive feature, the NMW voltammogram shows two reduction peaks: a major reduction pre-wave at ~-0.12 V and a minor shoulder around -0.55 V. This behavior reflects the co-existence of different active sites in the NMW carbon lattice and it is clearly maintained in the voltammograms of the NMW@N_{1-2} derivatives (Fig. 2A, curves b and c).[37] Their ORR performance (number of transferred electrons per O_2 molecule) in the diffusion and kinetically limited regions (from -0.65 to -0.95 V) is evaluated on the basis of the Koutecky–Levich (K–L) equation.[86,87]

The K–L plots of each catalytic system obtained at different potential values (from -0.65 to -0.95 V) are reported in Fig. S8 (see the ESI) and the calculated number of exchanged electrons ($n_E = -0.95$ V) per mol of O_2 is listed in Table 1.

Table 1. E_{on} values (V) and average number of e– transferred ($n_E = -0.95$ V) per O_2 molecule as derived from plots in Fig. 2, 4D and S8.

Entry	Catalyst	E_{on}(V)	n_E
1	Pt	-0.10	4.0
2	NMW	-0.12	3.9
3	NMW@$N_1^{(Py)}$	-0.24	2.2
4	NMW@$N_2^{(Acr)}$	-0.14	3.6
5	GC	-0.31	2.0
6	r-NMW	-0.16	3.6

Notably, the electrochemical behavior of the NMW@N_{1-2} samples is deeply influenced by the nature of the surface grafted N-groups. The surface grafted N-groups control both the E_{on} and n_E values (Table 1) whereas only a minor contribution to their performance can be ascribed to the

inherent N-doping at the NMW core. This result is additionally confirmed by comparing the electrochemical performance of the NMW@N$_{1,2}$ samples with that of "fully C" multi-walled carbon nanotubes (MWCNT) decorated with the same N-containing groups (MWCNT@N$_1^{(Py)}$ and MWCNT@N$_2^{(Acr)}$). As Fig. 3 shows, all materials featuring the same N-surface functionalities behave similarly, showing almost superimposable voltammetric profiles irrespective of the nature [doped (NMW) or undoped (MWCNT)] of the nanomaterial core (Fig. 3, curves g vs. b and c vs. f). On this basis, it can be inferred that chemical functionalization of NMW occurs on its main surface active sites (C-sites) responsible for the inherent material electrochemical properties and simply "switches them off".
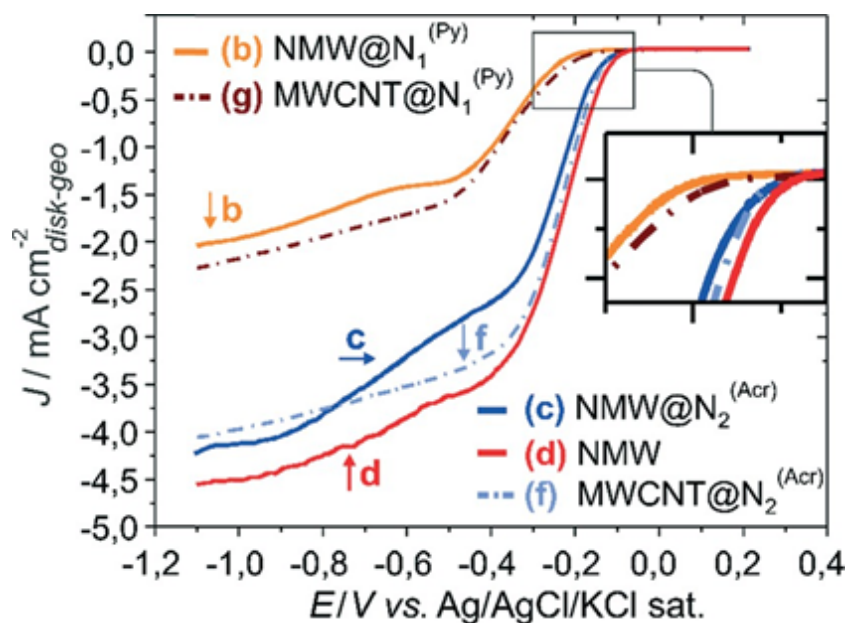

Figure 3. RRDE current–potential curves at 293 K for ORR in an O$_2$ saturated 0.1 M KOH solution recorded by using a rotating ring-disk GC electrode [GC disk, A = 0.196 cm^2]. All samples are measured at an angular rotation rate (f) of 800 rpm with a scan rate of 5 mV s^{-1}. Pt ring currents are omitted for the sake of simplicity.

As a result, the ORR at the functionalized NMW samples (NMW@N$_{1,2}$) is displaced on an upper material surface level, where dangling pyridine-based arms (pyridine or acridine) of- fer new active carbon sites for the process to occur. The electronic charge density distribution at the respective heterocycles finally controls the ability of the metal-free electrocatalysts to promote the dioxygen reduction more or less efficiently.[53,54] Comparison of the curves also unveils how the same N-

configuration (N-pyridinic) gives rise to electrocatalysts with different performances. Indeed, both E_{on} and J_D (Fig. 3, curves c and f vs. b and g) are largely affected by the nature of substituents on the pyridine dangling groups (e.g. pyridine vs. acridine). These new insights, along with the similarities between the electrochemical profiles of MWCNT@$N_2^{(Acr)}$ and plain NMW (Fig. 3, curves d vs. f), offer valuable clues to debate on the effective nature of the N-containing groups in the pristine NMW and their role in the performance of the catalyst in the ORR.

Although any conclusion on this point is always hard to be unambiguously addressed, our evidence fosters the hypothesis of acridine-like frameworks at the NMW graphitic planes[46,47,51] holding a key role in the electrocatalytic performance of NMW (E_{on} and J_D). Finally, the slightly better E_{on} and J_D values measured on NMW with respect to MWCNT@$N_2^{(Acr)}$ are ascribable to a more complex surface composition of the former. In fact, the work-up conditions applied to NMW[58] generate O-containing functionalities (–COOH, –OH, ethers) that deeply modify its electronic surface properties. As a result, the formation of O-defects improves the ability of the acridine-like frameworks in NMW to activate dioxygen. Further proof of evidence of that is given by the markedly worse electrochemical perfor- mance of NMW in its reduced form (r-NMW – see section 3.3).

3.3 Synthesis, characterization and electrocatalytic properties in ORR of reduced NMW (r-NMW)

To prepare the reduced r-NMW sample, NMW was subjected to a thermal treatment at 350 °C for 1 h under an inert atmosphere (Ar, 100 mL min^{-1}). These conditions are used to remove the more thermally labile O-containing species at the material surface while preserving as much as possible the overall N-content (in terms of both relative N% and N-configuration). Under these conditions, carboxylic acid groups rapidly decompose to CO_2 (ref. 88) as witnessed by the almost complete suppression of the CO_2 signal in the TPD-MS profile of r-NMW (Fig. 4A). TG analysis under air gave additional evidence of the surface modifications that occurred. As Fig. 4B shows, a higher weight loss is measured for the NMW sample compared to its reduced counterpart (r-NMW) in the

150–450 °C temperature range. EA qualitatively accounts for the removal of surface oxygen-containing groups with an in- creased carbon and nitrogen content (%) in r-NMW if compared with NMW (C: 94.7; N: 3.6 vs. C: 89.0; N: 3.2, respectively Table S1, see the ESI). Finally, the XPS N 1s spectrum of r-NMW (Fig. 4C) shows an almost superimposable profile to that of NMW (Fig. 1).
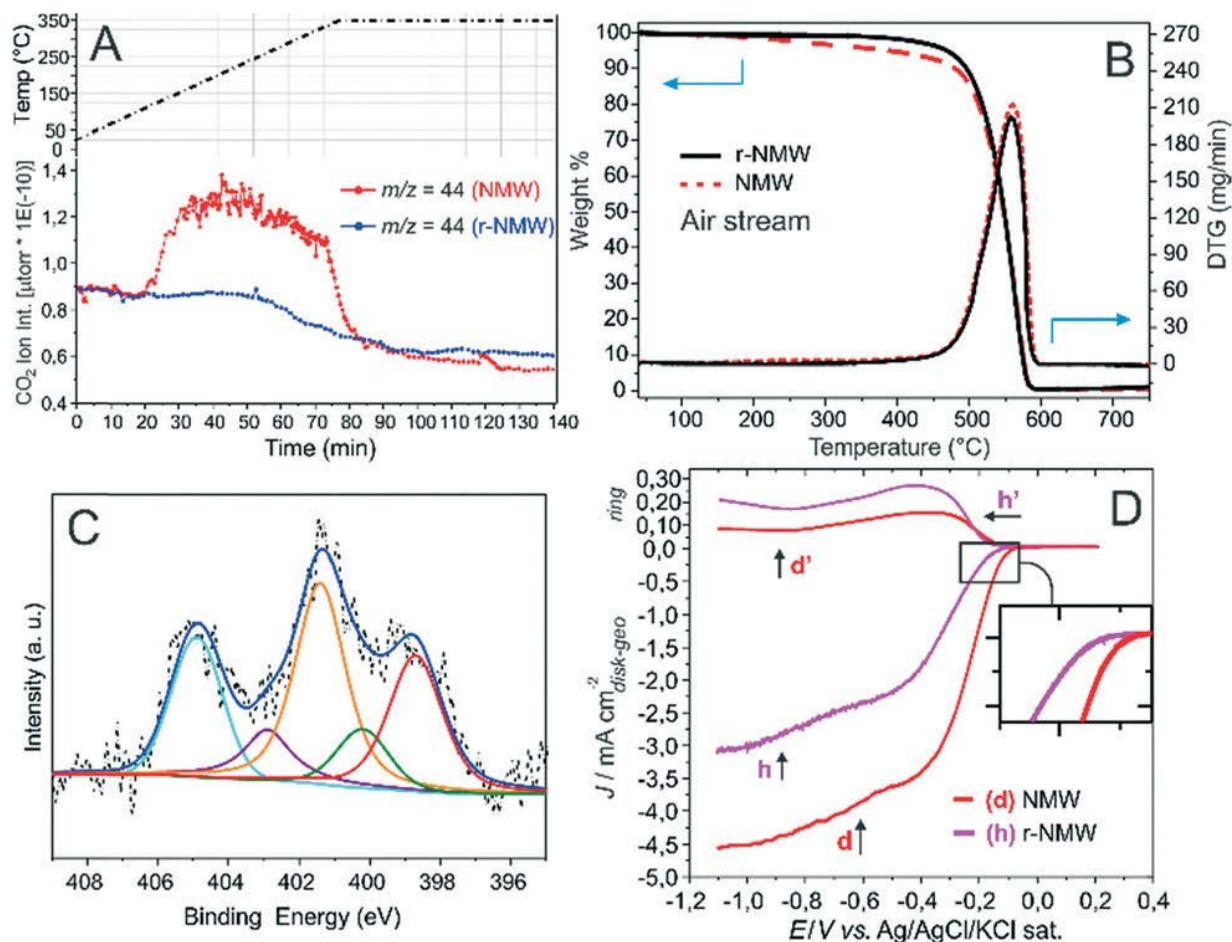

Figure 4. (A) TPD-MS analysis of NMW (red curve) and r-NMW (blue curve) samples, respectively. (B) TG/DTG profiles of NMW and r-NMW under air. Thermal conditions: 40–800 °C, 5 °C min^{-1} ; air 100 mL min^{-1}. (C) High resolution XPS N 1s core level region of r-NMW and its relative curve fitting. (D) RRDE current–potential curves at 293 K for ORR in an O2 saturated 0.1 M KOH solution. Samples are measured at an angular rotation rate (f) of 800 rpm with a scan rate of 5 mV s^{-1}. Pt ring [A = 0.11 cm^2] currents measured from 0.2 to −1.1 V, keeping the ring potential at 0.50 V.

All these data taken together confirm the negligible effects of the thermal treatment at 350 °C under an Ar atmosphere on the final N-composition of r-NMW. On the other hand, a significant change in its electronic properties invariably takes place because of the thermal removal of electron-withdrawing carboxylic groups from its outer surface.[88] This change is invoked to justify the markedly reduced ORR performance of r-NMW compared to that of its pristine counterpart (NMW).

Indeed, the E_{on} value measured for the r-NMW is negatively shifted (~ 40 mV) compared to that of NMW and the average number of electrons transferred per mol of O_2 (n_E at -0.95 V) drops down to 3.6 (Table 1 and Fig. 4D and S8).

This evidence confirms the central role played by electronic factors on the ability of the surface exposed N-functional groups engaged in the ORR. Indeed, materials showing the same N-configurations) and N-loading (i.e. NMW and r-NMW) but featuring different electronic surface properties offer different ORR performances.

As a complement to this experimental evidence, the truly metal-free nature of the ORR process promoted by either NMW or r-NMW has been demonstrated. As shown in Fig. 4B, after complete material combustion (>600 °C), negligible solid residues are recovered from both samples in equalamounts (largely below 1 wt%). These unburned solids are due to metal catalyst residues (FeO_x) not removed from the bulk material by the work-up treatment and not detectable by the XPS analysis (see survey spectra of NMW and r-NMW in Fig. S9, see the ESI). Despite their markedly different performances in ORR, metal leaching or nanoparticles sintering effects cannot be invoked as a consequence of the NMW treatment at 350 °C under Ar. Furthermore, the removal of thermally labile surface organic functionalities in r-NMW should enhance, in principle at least, the exposure of the surface metal nanoparticles to O_2, thus leading to electrocatalysts with improved ORR performance. In contrast, r-NMW is a worse electrocatalyst than NMW. This evidence excludes any contribution from surface exposed metal contaminants to their activity in the ORR.

3.4 Synthesis, characterization and electrocatalytic properties in ORR of the benchmark MWCNT@Acr^{OX} sample

The assumption of a unique N-configuration (i.e. basic acridine-like defects) controlling the ORR performance of NMW contrasts with its negligible surface basicity. Indeed, acid–base titration measurements (Table S2, see the ESI) on NMW give a 0.06 wt% of surface N-basic sites. This result can be easily explained by the fast oxidation of the outmost pyridinic-cores to their N-oxide

counterparts throughout the material work-up. This is mirrored by the appearance of XPS components at high binding energies in the XPS N 1s core region spectrum of NMW (Fig. 1). Indeed, the treatment of NMW in refluxing aqua regia irreversibly converts the basic pyridinic groups into their N-oxide counterparts. To shed light on the role of the N-oxide groups in ORR promoted by N-doped CNMs, the model acridine N-oxide functionalized sample MWCNT@Acr^{OX} has been prepared and tested as a benchmark N-oxide-based catalyst.

MWCNT@Acr^{OX} is prepared according to the functionalization protocol outlined in Scheme 2, taking care of adopting similar work-up procedures, blank test analyses and characterization tools already discussed for the above mentioned N-decorated NMW (NMW@N$_{1,2}$) samples.
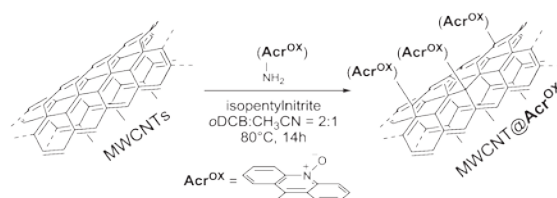
Scheme 2. MWCNTs functionalization with acridine N-oxide groups via aryldiazonium salt chemistry (Tour protocol).

The aniline N-oxide reagent (H$_2$N-Acr^{OX}) is obtained as an analytically pure bright red solid through a controlled oxidative treatment of the commercially available 9-aminoacridine (see the ESI). Qualitative evidence of the functionalization that occurred is provided by TG analysis (Fig. S10, see the ESI), while a quantitative estimation of the material N-loading is given by elemental analysis (Table S1) and N1s XPS data (Fig. 5D). Overall, the MWCNT@Acr^{OX} features a N-content of 0.42% (average value calculated from EA and XPS) and presents a characteristic N 1s profile featured by one main peak centered at 402.5 eV, consistent with N-pyridine-oxide nuclei [70,77,78](Fig. 5D). The CV on the MWCNT@Acr^{OX} has unveiled a rather complex electrochemical behavior. Measurements have been performed in a three-electrode cell operating in either a N$_2$- or an O$_2$-saturated 0.1 M KOH solution, sweeping potentials linearly from −1.1 to 0.2 V at a scan rate of 5 mVs^{-1}(vs. Ag/ AgCl/KCl sat.).
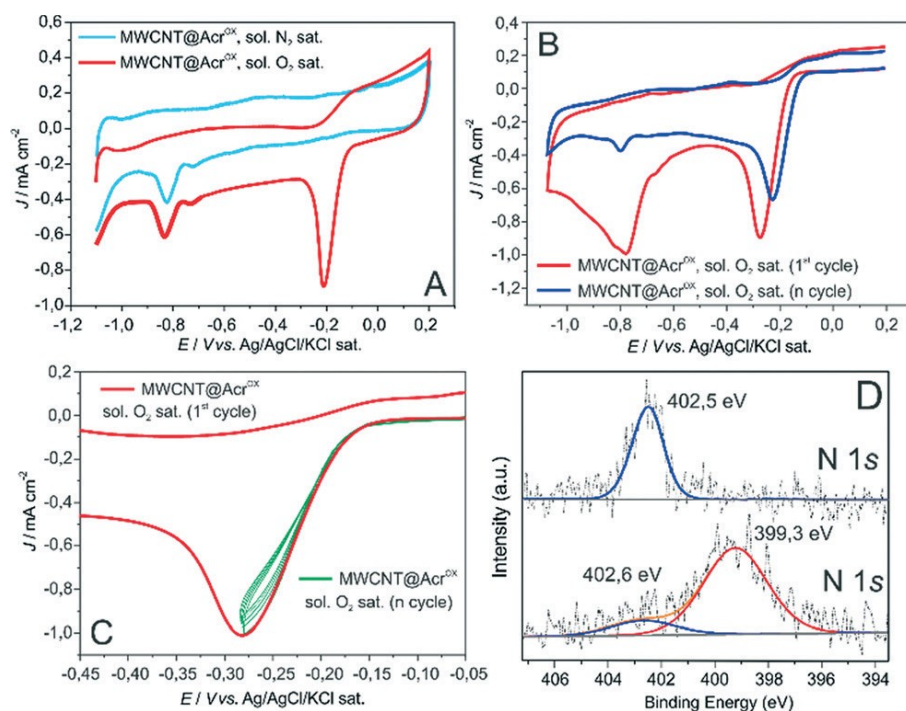
Figure 5. (A) Cyclic voltammograms of the MWCNT@Acr^{OX} sample under N$_2$-saturated (light blue-line) and O$_2$-saturated solutions (red-line), sweeping potentials linearly from −1.1 V to 0.2 V with a scan rate of 5 mV s^{-1}. (B) Cyclic voltammograms of the MWCNT@Acr^{OX} sample under an O$_2$-saturated solution, sweeping potentials linearly from 0.2 V to −1.1 V with a scan rate of 5 mV s^{-1}. First (red curve) and n (blue curve) voltammetric cycles. (C) Cyclic voltammograms on the MWCNT@Acr^{OX} sample under an O$_2$-saturated solution (red curve, first run). Green curves refer to the CV measured sweeping potentials linearly from 0.2 V to −0.28 V with a scan rate of 5 mV s^{-1}. (D) XPS high resolution N 1s core level regions and related fits of the MWCNT@Acr^{OX} sample before (top) and after (down) cyclic voltammetry in the 0.2 ÷ −1.1 V range of potentials.

As Fig. 5A shows, under O$_2$-saturated conditions, MWCNT@Acr^{OX} presents a marked and irreversible oxygen reduction peak not present under N$_2$-saturated conditions (red curve vs. light-blue one). Irrespective of the O$_2$- or N$_2$-saturated environment, a further irreversible reduction process takes place at higher overpotentials (~ −0.8 V) on both CV profiles. CV tests conducted under O$_2$-saturated conditions and operated by reversing the curve scan from oxidative to reductive potentials (from 0.2 to −1.1 V at a scan rate of 5 mV s^{-1}) have been used to get additional electrochemical insights. Fig. 5B illustrates the profiles of two selected CV scans recorded on a freshly prepared electrode. Although not representative of an electrochemical system under the regime conditions, the first CV (red curve) presents two marked peaks of reduction, the first being

unambiguously attributed to O_2 reduction ($E_{on} \approx -0.18$ V). Noteworthy, the second broader and intense reduction peak is definitively suppressed under the regime conditions (blue curve after ≥20 CVs in the $0.2 \div -1.1$ V range of potentials) and the E_{on} value associated with O_2 reduction is positively shifted of about 40 mV (−0.14 V vs. Ag/AgCl/KCl sat. – Fig. 5B red curve vs. the blue one).

Both aspects reflect a deep surface modification of the MWCNT@Acr^{OX} occurring at higher reducing potentials. This modification directly correlates with the observed positive E_{on} shifting. Indeed, when the potentials are swept in the narrower $0.2 \div -0.28$ V range, the E_{on} value of MWCNT@Acr^{OX} is constant at −0.18 V without any appreciable change in the electrochemical profile even after tens of voltammetric cycles (Fig. 5C). The disappearance of the second reduction peak together with the positive E_{on} shifting in the CV profile can be explained with the N-oxide conversion (Acr^{OX}) into plain N-groups (Acr), once MWCNT@Acr^{OX} is subjected to potentials more reducing than −0.6 V. This hypothesis is initially confirmed by the almost superimposable RRDE profiles of MWCNT@Acr^{OX} and MWCNT@Acr[53,54] both under the regime conditions (Fig S11, see the ESI). The electrode surface transformation that occurred is finally confirmed by the XPS analysis of the recovered MWCNT@Acr^{OX} catalyst after RRDE measurements (Fig. 5D, top vs. bottom). The N 1s XPS spectrum of the used electrocatalyst (bottom) shows one main component at 399.3 eV followed by an only minor shoulder at high binding energies (402.6 eV). While the former is attributed to pyridinic moieties,[68–71] the latter is ascribed to residues of the acridine N-oxide groups. Similar to MWCNT@Acr^{OX}, the N-oxide surface groups of NMW are readily transformed into free N-groups upon material exposure at reducing potentials. This also explains the negligible surface basicity measured on NMW, where the N-oxide groups initially present on its surface are reduced to their free N-analogues during the electrochemical experiments. This evidence is in line with the hypothesis of acridine-like defects as key-players controlling the ORR performance of the CVD prepared NMW sample.

4. Conclusions

To summarize, CVD-prepared N-doped CNMs (NMWs) and their N-decorated (chemically functionalized) counterparts (NMW@$N_{1,2}$) have been prepared and employed as metal-free electrocatalysts in ORR. The chemical functionalization process occurs on the NMW surface sites responsible for their inherent electrochemical properties and "switches them off". As a result, the oxygen reduction performed by the functionalized samples (NMW@$N_{1,2}$) is transferred to an upper surface level, where the dangling N-arms offer new active carbon sites for the process to occur. The electronic charge density distribution at the appended heterocycles (acridine, pyridine) finally controls the ability of the electrocatalysts to promote ORR more or less efficiently. The rational combination of CVD and chemical functionalization has been exploited to support the hypothesis of a unique N-configuration (N- pyridinic) holding an exclusive control on the catalyst E_{on} and J_D. This claim may be against some literature reports, where N-pyridinic sites improve the E_{on} values, whereas the control on J_D is commonly ascribed to the N-graphitic sites.[30] The careful analysis of the NMW surface properties along with a systematic comparison of the electrochemical outcomes of related benchmark systems (r-NMW, MWCNT@Acr, MWCNT@Acr^{ox}) fosters the idea of acridine-like groups within a favorable electronic environment holding a full control on the ORR performance of NMW. As a complement to this experimental work, the truly metal-free nature of the ORR process promoted by NMW has been demonstrated. Overall, chemical grafting with tailored N-functionalities is a powerful tool to unveil original electrochemical outcomes and to establish the real nature of N-groups engaged in ORR performed by complex carbon nanomaterials.

References

1. L. Dai, Y. Xue, L. Qu, H.-J. Choi and J.-B. Baek, Chem. Rev., 2015, 115, 4823–4892.

2. F. Cheng and J. Chen, Chem. Soc. Rev., 2012, 41, 2172–2192.

3. D.-W. Wang and D. Su, Energy Environ. Sci., 2014, 7, 576–591.

4. L. Feng, Y. Yan, Y. Chen and L. Wang, Energy Environ. Sci., 2011, 4, 1892–1899.

5. B. C. H. Steele and A. Heinzel, Nature, 2001, 414, 345–352.

6. E. Antolini, Appl. Catal., B, 2009, 88, 1–24.

7. Y. Shao, G. Yin and Y. Gao, J. Power Sources, 2007, 171, 558–566.

8. R. Borup, J. Meyers, B. Pivovar, Y. S. Kim, R. Mukundan, N. Garland, D. Myers, M. Wilson, F. Garzon, D. Wood, P. Zelenay, K. More, K. Stroh, T. Zawodzinski, J. Boncella, J. E. McGrath, M. Inaba, K. Miyatake, M. Hori, K. Ota, Z. Ogumi, S. Miyata, A. Nishikata, Z. Siroma, Y. Uchimoto, K. Yasuda, K.-I. Kimijima and N. Iwashita, Chem. Rev., 2007, 107, 3904–3951.

9. S. Zhang, X. Yuan, H. Wang, W. Mérida, H. Zhu, J. Shen, S. Wu and J. Zhang, Int. J. Hydrogen Energy, 2009, 34, 388–404.

10. A. Morozan, B. Jousselme and S. Palacin, Energy Environ. Sci., 2011, 4, 1238–1254.

11. Y. Zheng, Y. Jiao, M. Jaroniec, Y. G. Jin and S. Z. Qiao, Small, 2012, 8, 3550–3566.

12. C. Z. Zhu and S. J. Dong, Nanoscale, 2013, 5, 1753–1767.

13. D. Yu, E. Nagelli, F. Du and L. Dai, J. Phys. Chem. Lett., 2010, 1, 2165–2173.

14. C. Song and J. Zhang, in PEM Fuel Cell Electrocatalysts and Catalyst Layers: Fundamentals and Applications, ed. J. Zhang, Springer, New York, 2008, pp. 89–134.

15. D. S. Su, S. Perathoner and G. Centi, Chem. Rev., 2013, 113, 5782–5816.

16. K. Gong, F. Du, Z. Xia, M. Durstock and L. Dai, Science, 2009, 323, 760–764.

17. Y. Gao, G. Hu, J. Zhong, Z. Shi, Y. Zhu, D. S. Su, J. Wang, X. Bao and D. Ma, Angew. Chem., Int. Ed., 2013, 52, 2109–2113.

18. J. Zhang and L. Dai, ACS Catal., 2015, 5, 7244–7253.

19. Y. Li, W. Zhou, H. L. Wang, L. M. Xie, Y. Y. Liang, F. Wei, J. C. Idrobo, S. J. Pennycook and

H. Dai, Nat. Nanotechnol., 2012, 7, 394–400.

20. B. B. Blizanac, P. N. Ross and N. M. Markovic, Electrochim. Acta, 2007, 52, 2264–2271.

21. J. Shui, M. Wang, F. Du and L. Dai, Sci. Adv., 2015, 1, e1400129.

22. P. Wang, Z. Wang, L. Jia and Z. Xiao, Phys. Chem. Chem.Phys., 2009, 11, 2730–2740.

23. Z. Luo, S. Lim, Z. Tian, J. Shang, L. Lai, B. MacDonald, C. Fu, Z. Shen, T. Yu and J. Lin, J. Mater. Chem., 2011, 21, 8038–8044.

24. X. Hu, Y. Wu, H. Li and Z. Zhang, J. Phys. Chem. C, 2010, 114, 9603–9607.

25. T. Ikeda, M. Boero, S.-F. Huang, K. Terakura, M. Oshima and J.-I. Ozaki, J. Phys. Chem. C, 2008, 112, 14706–14709.

26. D. M. Guldi and N. Martin, Carbon Nanotubes and Related Structures Synthesis, Characterization, Functionalization, and Applications, Wiley-VCH, Weinheim, 2010.

27. Y. Zhang, L. Zhang and C. Zhou, Acc. Chem. Res., 2013, 46, 2329–2339.

28. C. D. Higgins, J. Wu, W. Li and Z. Chen, Electrochim. Acta, 2012, 59, 8–13.

29. S. M. Unni, S. Devulapally, N. Karjulea and S. Kurungot, J. Mater. Chem., 2012, 22, 23506–3513.

30. L. Lai, J. R. Potts, D. Zhan, L. Wang, C. K. Poh, C. Tang, H. Gong, Z. Shen, J. Lin and R. S. Ruoff, Energy Environ. Sci., 2012, 5, 7936–7942.

31. H. Yang, C. Shan, F. Li, D. Han, Q. Zhang and L. Niu, Chem. Commun., 2009, 3880–3882.

32. S. Park, Y. Hu, Y. O. Hwang, S. E. Lee, L. B. Casabianca, W. Cai, J. R. Potts, H. W. Ha, S. Chen, J. Oh, S. O. Kim, Y. H. Kim, Y. Ishii and R. S. Ruoff, Nat. Commun., 2012, 3, 638–645.

33. T.-P. Fellinger, F. Hasché, P. Strasser and M. Antonietti, J. Am. Chem. Soc., 2012, 134, 4072–4075.

34. K. Ai, Y. Liu, C. Ruan, L. Lu and G. Lu, Adv. Mater., 2013, 25, 998–1003.

35. H. Li, W. Kang, L. Wang, Q. Yue, S. Xu, H. Wang and J. Liu, Carbon, 2013, 54, 249–257.

36. S. Kundu, T. C. Nagaiah, W. Xia, Y. Wang, S. Van Dommele, J. H. Bitter, M. Santa, G. Grundmeier, M. Bron, W. Schuhmann and M. Muhler, J. Phys. Chem. C, 2009, 113, 14302–14310.

37. C. V. Rao, C. R. Cabrera and Y. Ishikawa, J. Phys. Chem. Lett., 2010, 1, 2622–2627.

38. N. P. Subramanian, X. Li, V. Nallathambi, S. P. Kumaraguru, H. Colon-Mercado, G. Wu, J.-W. Lee and B. N. Popov, J. Power Sources, 2009, 188, 38–44.

39. K. Y. Park, J. H. Jang, J. E. Hong and Y. U. Kwon, J. Phys. Chem. C, 2012, 116, 16848–16853.

40. C. Jeyabharathi, P. Venkateshkumar, M. S. Rao, J. Mathiyarasu and K. L. N. Phani, Electrochim. Acta, 2012, 74,171–175.

41. H. Niwa, K. Horiba, Y. Harada, M. Oshima, T. Ikeda, K. Terakura, J.-I. Ozaki and S. Miyata, J. Power Sources, 2009, 187, 93–97.

42. B. Zheng, J. Wang, F. B. Wang and X. H. Xia, Electrochem. Commun., 2013, 28, 24–26.

43. M. Chokai, M. Taniguchi, S. Moriya, K. Matsubayashi, T. Shinoda, Y. Nabae, S. Kuroki, T. Hayakawa, M. Kakimoto, J. Ozaki and S. Miyata, J. Power Sources, 2010, 195,5947–5951.

44. A. Morozan, P. Jégou, M. Pinault, S. Campidelli, B. Jousselme and S. Palacin, ChemSusChem, 2012, 5, 647–651.

45. D. Geng, Y. Chen, Y. Chen, Y. Li, R. Li, X. Sun, S. Ye and S. Knights, Energy Environ. Sci., 2011, 4, 760–764.

46. T. Sharifi, G. Hu, X. Jia and T. Wågberg, ACS Nano, 2012, 10, 8904–8912.

47. E. J. Biddinger and U. S. Ozkan, J. Phys. Chem. C, 2010, 114,15306–15314.

48. A. Zhao, J. Masa, M. Muhler, W. Schuhmann and W. Xia, Electrochim. Acta, 2013, 98, 139–145.

49. D. Deng, X. Pan, L. Yu, Y. Cui, Y. Jiang, J. Qi, W.-X. Li, Q. Fu, X. Ma, Q. Xue, G. Sun and X. Bao, Chem. Mater., 2011, 23, 1188–1193.

50. Y. Zhang, J. Ge, L. Wang, D. Wang, F. Ding, X. Tao and W. Chen, Sci. Rep., 2013, 3, 2771–2779.

51. P. H. Matter, L. Zhang and U. S. Ozkan, J. Catal., 2006, 239, 83–96.

52. R. A. Sidik, A. B. Anderson, N. P. Subramanian, S. P. Kumaraguru and B. N. Popov, J. Phys. Chem. B, 2006, 110, 1787–1793.

53. G. Tuci, C. Zafferoni, P. D'Ambrosio, S. Caporali, M. Ceppatelli, A. Rossin, T.

Tsoufis, M. Innocenti and G. Giambastiani, ACS Catal., 2013, 3, 2108–2111.

54. G. Tuci, C. Zafferoni, A. Rossin, A. Milella, L. Luconi, M. Innocenti, L. Truong Phuoc, C. Duong-Viet, C. Pham-Huu and G. Giambastiani, Chem. Mater., 2014, 26, 3460–3470.

55. L. Wang, A. Ambrosi and M. Pumera, Angew. Chem., Int. Ed., 2013, 52, 13818–13821.

56. K. Parvez, S. Yang, Y. Hernandez, A. Winter, A. Turchanin, X. Feng and K. Müllen, ACS Nano, 2012, 6, 9541–9550.

57. D. D. Perrin, W. L. F. Armarego and D. R. Perrin, Purification of Laboratory Chemicals, Pergamon, New York, 2nd ed. edn., 1980.

58. K. Chizari, A. Deneuve, O. Ersen, I. Florea, Y. Liu, D. Edouard, I. Janowska, D. Begin and C. Pham-Huu, ChemSusChem, 2012, 5, 102–108.

59. A. P. Schuetze, W. Lewis, C. Brown and W. j. Geerts, Am. J. Phys., 2004, 72, 149–153.

60. M. Ceppatelli, F. A. Gorelli, J. Haines, M. Santoro and R. Bini, Z. Kristallogr., 2014, 229, 83–91.

61. A. C. Ferrari and J. Robertson, Phys. Rev. B: Condens. Matter Mater. Phys., 2000, 61, 14095–14107.

62. A. C. Ferrari and J. Robertson, Phys. Rev. B: Condens. Matter Mater. Phys., 2001, 64, 075414–075426.

63. M. M. Lucchese, F. Stavale, E. H. Martins Ferreira, C. Vilani, M. V. O. Moutinho, R. B. Capaz, C. A. Achete and A. Jorio, Carbon, 2010, 48, 1592–1597.

64. S. Treimer, A. Tang and D. C. Johnson, Electroanalysis, 2002, 14, 165–171.

65. K. C. Waugh, Appl. Catal., 1988, 43, 315–337.

66. B. Ballesteros, G. de la Torre, C. Ehli, G. M. Aminur Rahman, F. Agulló-Rueda, D. M. Guldi and T. Torres, J. Am. Chem. Soc., 2007, 129, 5061–5068.

67. E. Moaseri, M. Baniadam, M. Maghrebi and M. Karimi, Chem. Phys. Lett., 2013, 555, 164–167.

68. Y. F. Zhao, L. Zhao, K. X. Yao, Y. Yang, Z. Q. and Y. Han, J. Mater. Chem., 2012, 22, 19726–19731.

69. M. C. Gutierrez, D. Carriazo, C. O. Ania, J. B. Parra, M. L. Ferrer and F. del Monte, Energy Environ. Sci., 2011, 4, 3535–3544.

70. X. Q. Wang, C. G. Liu, D. Neff, P. F. Fulvio, R. T. Mayes, A. Zhamu, Q. Fang, G. R. Chen, H. M. Meyer, B. Z. Jang and S. Dai, J. Mater. Chem. A, 2013, 1, 7920–7926.

71. J. C. Wang, I. Senkovska, M. Oschatz, M. R. Lohe, L. Borchardt, A. Heerwig, Q. Liu and S. Kaskel, ACS Appl. Mater. Interfaces, 2013, 5, 3160–3167.

72. G. P. Hao, W. C. Li, D. Qian and A. H. Lu, Adv. Mater., 2010, 22, 853–857.

73. P. Nowicki, R. Pietrzak and H. Wachowska, Energy Fuels, 2010, 24, 1197–1206.

74. D. N. Hendrickson, J. M. Hollander and W. L. Jolly, Inorg. Chem., 1969, 8, 2642–2647.

75. X. Y. Ma, M. H. Cao and C. W. Hu, J. Mater. Chem. A, 2013, 1, 913–918.

76. J. Wei, D. D. Zhou, Z. K. Sun, Y. H. Deng, Y. Y. Xia and D. Y. Zhao, Adv. Funct. Mater., 2013, 23, 2322–2328.

77. J. L. Bahr and J. M. Tour, Chem. Mater., 2001, 13, 3823–3824.

78. C. D. Doyle and J. M. Tour, Carbon, 2009, 47, 3215–3218.

79. C. A. Dyke, M. P. Stewart, F. Maya and J. M. Tour, Synlett, 2004, 155–160.

80. C. A. Dyke and J. M. Tour, J. Am. Chem. Soc., 2003, 125, 1156–1157.

81. C. A. Dyke and J. M. Tour, Nano Lett., 2003, 3, 1215–1218.

82. J. L. Hudson, M. J. Casavant and J. M. Tour, J. Am. Chem.Soc., 2004, 126, 11158.

83. B. K. Price, J. L. Hudson and J. M. Tour, J. Am. Chem. Soc., 2005, 127, 14867–14870.

84. B. K. Price and J. M. Tour, J. Am. Chem. Soc., 2006, 128, 12899–12904.

85. S. van Dommele, K. P. De Jong and J. H. Bitter, Chem. Commun., 2006, 4859–4861.

86. Y. Wang, D. Zhang and H. Liu, J. Power Sources, 2010, 195, 3135–3139.

87. A. J. Bard and L. R. Faulkner, Electrochemical Methods: Fundamentals and Applications, 2nd edn., 2001.

88. P. Brender, R. Gadiou, J.-C. Rietsch, P. Fioux, J. Dentzer, A. Ponche and C. Vix-Guterl, Anal. Chem., 2012, 84, 2147–2153.